Motion Estimation Under Location Uncertainty, Application To Large-Scale Characterization Of A Mixing Layer

Romain Schuster, Dominique Heitz, Etienne Mémin

Motion Estimation Under Location Uncertainty, Application To Large-Scale Characterization Of A Mixing Layer

Romain Schuster[1,2,3*], Dominique Heitz[2,3], Etienne Mémin[3]

1: Institut Technique des Gaz et de l'Air, Rue de la Terre Adélie Parc Edonia Bâtiment R, 35768 Saint-Grégoire, France
2: Irstea, UR OPAALE, Rennes Cedex F-35044, France
3: INRIA, Fluminance group, Campus Universitaire de Beaulieu, Rennes Cedex F-35042, France
* Correspondent author: romain.schuster@irstea.fr

Keywords: Large-scale PIV, Optical Flow, Stochastic Modeling, Mixing Layer

ABSTRACT

We propose a novel motion estimation from image sequences method to study turbulent flows. This method consists in modeling the luminance motions between successive frames as a new stochastic scalar transport equation. Thanks to stochastic formalism the motion field is separated into a large-scale smooth component and a random small-scale component. This decomposition gives rise to the mentioned new stochastic transport equation that takes into account the interactions between observed large scales and unresolved ones. This equation provides a new data term for optical flow algorithm. We then resolved the aperture problem with local Lucas-Kanade approach. We show that the method improves the motion estimation on a synthetic case. Then the method is tested on real large-scale observations of a mixing layer. Two kinds of tracers are compared and a new lighting system based on LED technology is employed to perform this large-scale experiment.

1. Introduction

The increasing necessity to understand and control indoor airflows requires the development of new tools or methods that can describe exhaustively flow features inside buildings. To develop such methods we naturally think about performing particle image velocimetry (PIV) inside buildings. As a matter of fact PIV is a very performant method developed and used in research laboratories to characterize fluid flows. A detailed description on advanced PIV principles can be found in the text book (Adrian, 1991). However PIV has been designed and optimized to study flows under control. Its transposition to study free flows inside buildings is not immediate. Several difficulties appear when we try to perform it in situ in real conditions. Firstly, the dimensions of fields that we want to investigate inside buildings are generally really bigger ($\geq 1m^2$) than those that are usually investigated in research laboratories. To allow this, it is naturally

possible to increase the number of cameras as already tested by (Lee et al., 2011). Actually it will make the set-up more complex and we aim at making it simple. Another option is to move backward the camera in order to extend the investigated area. Naturally by doing this the resolution will decrease. Particles within the image will appear smaller and the scattered light will be weakened. To overcome this problem, bigger particles like helium filled soap bubbles (HFSB) can be used. As a matter of fact these particles are brighter and follow the flow with a high fidelity (Scarano et al., 2015). This tracer is becoming widely used for large-scale applications. Another option is to use dense smoke seeding. By following smoke density gradients movements it is possible to retrieve quite well the velocity. In both cases the combination of this type of tracer with an expansion of the field of interest leads to a large-scale observation of the flow. Then motion estimation from image sequences has to be adapted. Usually velocity fields are extracted from image sequences by performing cross-correlation between successive images. It is a robust technique but it only provides large-scale velocity fields due to the size of interrogation windows. Moreover cross-correlation is not suited for smoke images, especially when luminance gradients are weak (Heitz et al., 2010). Optical flow is a motion estimation technique which comes from the computer vision community and was first introduced by (Horn and Schunck, 1981). Initially it was based on the hypothesis of luminance consistency during motion. This hypothesis gives rise to the optical flow constraint equation (1) also called data term that links luminance $I(\boldsymbol{x}, t)$ variations to the motion field $\boldsymbol{u}(\boldsymbol{x}, t)$ such that

$$\frac{\partial I}{\partial t} + \boldsymbol{u} \cdot \boldsymbol{\nabla} I = 0 \tag{1}$$

Optical flow technique computes a dense motion field (1 vector/pixel) so the resolution is higher compared to cross-correlation. When the brightness consistency hypothesis is well suited for rigid motions, it is not enough elaborate to cope with fluid motions. Then several attempts to improve fluid motion estimation using an optical flow approach were performed and have been reported in the review of (Heitz et al., 2010). Still with the goal of providing a more accurate estimation of fluid motion we have to consider a specific aspect of fluid flows which present a multi-scale behavior. As a matter of fact, due to camera frame rate and size of the field of view the spatio-temporal resolution is often too weak to see the small scales of the flow. This is even more true when smoke is used as a tracer. We cannot see unresolved scales but we have to model it to have a better estimation of coarser ones. A few works has been dedicated to the modeling of subgrid scales for motion estimation. This field was first adressed by (Cassisa et al., 2011) who introduced a data term based on passive scalar transport equation where the action of

unresolved scales is modeled by a trubulent diffusion computed a priori. If the estimation is improved, the main drawback of this approach comes from the necessity to know the power spectrum of the flow to compute the turbulent diffusion which is not necessarily known. In the continuation of this work (Zillé et al., 2014) proposed to model subgrid scales action during the multi-resolution process. Two options are exposed. The first one is a two-step procedure where the velocity field is computed once without subgrid modeling. Thanks to this motion field the subgrid scales are assessed and taken into account during the second step. The other option uses a subgrid scales model based on Smagorinsky coefficient. Despite the improvement they bring these strategies are strongly dissipative. Finally (Chen et al., 2015) improved the model of (Cassisa et al., 2011) using mix models introduced in LES by (Bardina et al., 1980).

In this paper we propose a new approach to derive scales interactions and improve motion estimation. This approach is based on (Mémin, 2014) work who decomposed the Eulerian flow velocity field into a large-scale smooth component and a rough small-scale turbulent component. Given this new random field (Resseguier et al., 2016) derived a new stochastic transport equation for a passive scalar that we will use as our new optical flow data term.

The rest of this article is organized as follows. In Sect. 2, the optical flow formulation under location uncertainty is derived in detail. Then evaluation on synthetic images is performed. To finish an experimental evaluation on a mixing layer is demonstrated and discussed.

2. Methodology description

2.1 Data term based on stochastic transport

Hereafter we will use the following notations :

- $\mathbb{R}^2$, for the image domain;
- $f: \mathbb{R}^+ \to \mathbb{R}^+$, will be a stochastic process representing the image luminance;
- $\boldsymbol{X}_t(x): \Omega \times \mathbb{R}^+ \to \Omega$, will be a stochastic process representing the Lagrangian trajectory of a particle located at x at the time $t = 0$ ($\boldsymbol{X}_0(x) = x$);

The model introduced by (Mémin, 2014) is based on a decomposition of the Eulerian velocity field into two components :

$$\boldsymbol{v} = \boldsymbol{w} + \boldsymbol{\sigma}\dot{\boldsymbol{B}}, \tag{2}$$

where

- $\boldsymbol{w}$, is a smooth large-scale component,

- $\dot{\boldsymbol{B}}$, is a random small-scale component, rapidly decorrelated in time, correlated in space, Gaussian, inhomogeneous and anisotropic, modeled by a Brownian process in time and a white noise process in space.

A particle transported in this stochastic Eulerian velocity field will have the following stochastic Lagrangian infinitesimal displacement :

$$\mathrm{d}\boldsymbol{X}_t = \boldsymbol{w}(\boldsymbol{X}_t, t)\mathrm{d}t + \boldsymbol{\sigma}(\boldsymbol{X}_t, t)\mathrm{d}\boldsymbol{B}_t, \tag{3}$$

where $\boldsymbol{\sigma}(\boldsymbol{X}_t, t)$ is a diffusion operator that specifies the spatial correlations of the velocity uncertainty.

The conservation of a scalar quantity implies that the material derivative has to be equal to zero. To express this material derivative (Resseguier et al., 2016) introduced a stochastic transport operator. Assuming that the luminance is proportional to the scalar density (Liu and Shen, 2008), we can use this transport operator to express the luminance transport which is given by :

$$\mathrm{d}_t f + (\boldsymbol{w}^*\mathrm{d}t + \boldsymbol{\sigma}\mathrm{d}\boldsymbol{B}_t)\cdot\boldsymbol{\nabla} f - \boldsymbol{\nabla}\cdot\left(\frac{1}{2}\boldsymbol{a}\boldsymbol{\nabla} f\right)\mathrm{d}t = 0, \tag{4}$$

where $\boldsymbol{w}^* = \boldsymbol{w} - \frac{1}{2}\boldsymbol{\nabla}\cdot\boldsymbol{a}$ is a modified large-scale velocity component due to small-scale inhomogeneities.

The first term of the left-hand side of (4) is the temporal increment of f. The second term is the advection by both modified large-scale velocity and random small-scale velocity. The third term is a diffusion term where $\boldsymbol{a} = (\boldsymbol{\sigma}\boldsymbol{\sigma}^T)$ is the diffusion tensor. Notice that the mathematical expectation of (4) is given by :

$$\mathbb{E}\left\{\mathrm{d}_t f + \boldsymbol{w}^*\mathrm{d}t\cdot\boldsymbol{\nabla} f - \boldsymbol{\nabla}\cdot\left(\frac{1}{2}\boldsymbol{a}\boldsymbol{\nabla} f\right)\mathrm{d}t\right\} = 0, \tag{5}$$

because the mathematical expectation of a Brownian process is null. So we obtain a new optical flow data term from (4). This single equation is not enough to estimate the motion field (a single equation for two unknown components). To solve this ill-posed problem we are looking for the velocity $\widehat{\boldsymbol{w}^*}$ which minimizes :

$$\mathbb{E}\left\{\left(\mathrm{d}_t f + (\boldsymbol{w}^* dt + \boldsymbol{\sigma} d\boldsymbol{B}_t)\cdot\boldsymbol{\nabla} f - \boldsymbol{\nabla}\cdot\left(\frac{1}{2}\boldsymbol{a}\boldsymbol{\nabla} f\right)dt\right)^2\right\}.$$

We use the local Lucas-Kanade (Lucas and Kanade, 1981) resolution technique where the mathematical expectation can be seen as a Gaussian spatial filter g_{σ_l}, σ_l defining the size of the local interrogation window. Then it is easy to show that the minimization of

$$\mathbb{E}\left\{\left(\mathrm{d}_t f + (\boldsymbol{w}^* dt + \boldsymbol{\sigma} d\boldsymbol{B}_t)\cdot \boldsymbol{\nabla} f - \boldsymbol{\nabla}\cdot\left(\frac{1}{2}\boldsymbol{a}\boldsymbol{\nabla} f\right) dt\right)^2\right\},$$

with respect to $\boldsymbol{w}^*$ assumed locally constant is equivalent to the minimization of

$$g_{\sigma_l} * \left[\mathrm{d}_t f + (\boldsymbol{w}^* dt + \boldsymbol{\sigma} d\boldsymbol{B}_t)\cdot \boldsymbol{\nabla} f - \boldsymbol{\nabla}\cdot\left(\frac{1}{2}\boldsymbol{a}\boldsymbol{\nabla} f\right) dt\right]^2.$$

This latter leads to a linear system of two equations for two unknowns whose solution is given by :

$$\begin{bmatrix}\widehat{u^*}\\ \widehat{v^*}\end{bmatrix} = \left(g_{\sigma_l} * \begin{bmatrix}\left(\frac{\partial f}{\partial x}\mathrm{d}t\right)^2 & \left(\frac{\partial f}{\partial x}\frac{\partial f}{\partial y}\right)\mathrm{d}t^2\\ \left(\frac{\partial f}{\partial x}\frac{\partial f}{\partial y}\right)\mathrm{d}t^2 & \left(\frac{\partial f}{\partial y}\mathrm{d}t\right)^2\end{bmatrix}\right)^{-1} \times \left(g_{\sigma_l} * \begin{bmatrix}-\left(\frac{\partial f}{\partial x}\mathrm{d}t\right)\left(\mathrm{d}_t f - \nabla\cdot\left(\frac{1}{2}\boldsymbol{a}\boldsymbol{\nabla} f\right)\mathrm{d}t\right)\\ -\left(\frac{\partial f}{\partial y}\mathrm{d}t\right)\left(\mathrm{d}_t f - \nabla\cdot\left(\frac{1}{2}\boldsymbol{a}\boldsymbol{\nabla} f\right)\mathrm{d}t\right)\end{bmatrix}\right). \quad (6)$$

2.2 Diffusion tensor estimation

The choice of the uncertainty model can be varied. We chose to begin with two simple models : an isotropic diffusion and an anisotropic one without cross terms. Hence, in the isotropic case the diffusion tensor $\boldsymbol{a}(\boldsymbol{x})$ takes the form below :

$$\begin{pmatrix}\alpha(\boldsymbol{x}) & 0\\ 0 & \alpha(\boldsymbol{x})\end{pmatrix},$$

with the condition $\alpha(\boldsymbol{x})^2 \geq 0$ because $\boldsymbol{a}(\boldsymbol{x})$ has to be symmetric positive definite. Under the assumption of a local homogeneity of $\boldsymbol{a}(\boldsymbol{x})$ in a close neighborhood of the investigated pixel, the equation (4) becomes :

$$\mathrm{d}_t f + (\boldsymbol{w}^*\mathrm{d}t + \boldsymbol{\sigma}\mathrm{d}\boldsymbol{B}_t)\cdot\boldsymbol{\nabla} f - \boldsymbol{\nabla}\cdot\left(\frac{1}{2}\alpha\Delta f\right)\mathrm{d}t = 0. \quad (7)$$

Then we estimate α locally by minimizing the expectation of the squared left-hand side of (7) with respect to α, which gives :

$$\widehat{\alpha} = \frac{2}{g_{\sigma_l} * (\Delta f \mathrm{d}t)^2} \times g_{\sigma_l} * [(\mathrm{d}_t f + \boldsymbol{w}^* \mathrm{d}t \cdot \nabla f)\Delta f \mathrm{d}t]. \tag{8}$$

In the case of an anisotropic diffusion, tensor $\boldsymbol{a}(\boldsymbol{x})$ takes the following form :

$$\begin{pmatrix} \alpha_1(\boldsymbol{x}) & 0 \\ 0 & \alpha_2(\boldsymbol{x}) \end{pmatrix},$$

with the condition $\alpha_1(\boldsymbol{x})\alpha_2(\boldsymbol{x}) \geq 0$ because $\boldsymbol{a}(\boldsymbol{x})$ has to be symmetric positive definite.With a similar assumption as used for the isotropic case, the equation (4) becomes :

$$\mathrm{d}_t f + (\boldsymbol{w}^* \mathrm{d}t + \boldsymbol{\sigma} \mathrm{d}\boldsymbol{B}_t) \cdot \boldsymbol{\nabla} f - \left(\frac{1}{2} \left(\alpha_1 \frac{\partial^2 f}{\partial x^2} + \alpha_2 \frac{\partial^2 f}{\partial y^2} \right) \right) \mathrm{d}t = 0. \tag{9}$$

Then we estimate (α_1, α_2) locally by minimizing the expectation of the squared left-hand side of (9) with respect to (α_1, α_2), which gives rise to a linear system (10) that we solve thanks to the Cramer rule :

$$\begin{bmatrix} \widehat{\alpha_1} \\ \widehat{\alpha_2} \end{bmatrix} = \left(g_{\sigma_l} * \begin{bmatrix} \frac{1}{2}\left(\frac{\partial^2 f}{\partial x^2}\mathrm{d}t\right)^2 & \frac{1}{2}\left(\frac{\partial^2 f}{\partial x^2}\frac{\partial^2 f}{\partial y^2}\right)\mathrm{d}t^2 \\ \frac{1}{2}\left(\frac{\partial^2 f}{\partial x^2}\frac{\partial^2 f}{\partial y^2}\right)\mathrm{d}t^2 & \frac{1}{2}\left(\frac{\partial^2 f}{\partial y^2}\mathrm{d}t\right)^2 \end{bmatrix} \right)^{-1} \times \left(g_{\sigma_l} * \begin{bmatrix} \left(\frac{\partial^2 f}{\partial x^2}\mathrm{d}t\right)(\mathrm{d}_t f + \boldsymbol{w}^* \mathrm{d}t \cdot \boldsymbol{\nabla} f) \\ \left(\frac{\partial^2 f}{\partial y^2}\mathrm{d}t\right)(\mathrm{d}_t f + \boldsymbol{w}^* \mathrm{d}t \cdot \boldsymbol{\nabla} f) \end{bmatrix} \right). \tag{10}$$

A more complex form of the diffusion matrix can be considered. It is currently under investigation but we can already say that it gives rise to a complex and time-consuming constrained minimization problem.

3. Validation with synthetic images

3.1 Tutrb2D sequence

In order to evaluate our novel motion estimation method we use synthetic images database « Turb2D » coming from the FLUID project (Heitz et al., 2007). This database contains 256×256 particle and scalar images, see figure 1. Within these images, particles and scalar are transported by a 2D homogeneous and isotropic turbulent flow with Reynolds number Re = 3000 and Schmidt number Sc = 0.7. This flow has been generated by a DNS (Carlier and Wieneke, 2005).

As we perfectly know the flow which transported the particles and the scalar, we can compare our estimation with the groundtruth velocity field. By this way we can evaluate the performances of our motion estimation method.

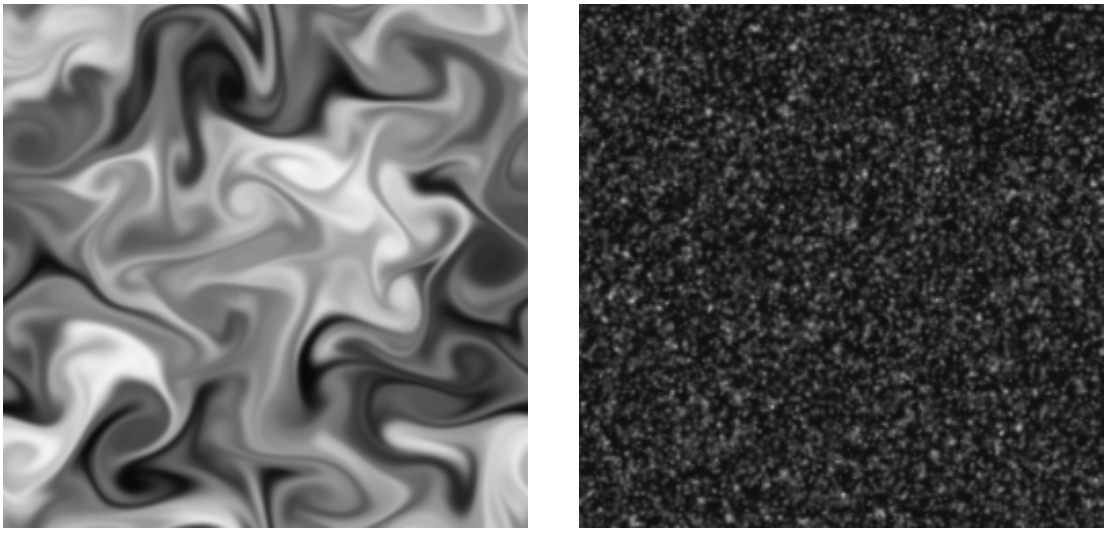

(a) Scalar image (b) Particle Image

Fig 1 Synthetic images of scalar (left) and particles (right) extracted from turb2D sequence of the FLUID project (Heitz et al., 2007).

3.2 Evaluation criteria

In order to assess statistically the performances of our motion estimation method we use as validation criteria the averaged magnitude error « Root Mean Square Error (RMSE) », the averaged angular error « Average Angular Error (AAE) » and the « Average Vorticity Error (AVE) ». Here are their mathematical definition :

$$RMSE(t) = \sqrt{\frac{1}{N}\sum_{\boldsymbol{x}\in\Omega} \|\boldsymbol{u_c}(\boldsymbol{x},t) - \boldsymbol{u_e}(\boldsymbol{x},t)\|^2}, \tag{11}$$

$$AAE(t) = \frac{1}{N}\sum_{\boldsymbol{x}\in\Omega} \cos^{-1}\left(\frac{\boldsymbol{u_c}(\boldsymbol{x},t)\cdot\boldsymbol{u_e}(\boldsymbol{x},t)}{\|\boldsymbol{u_c}(\boldsymbol{x},t)\|\|\boldsymbol{u_e}(\boldsymbol{x},t)\|}\right), \tag{12}$$

$$AVE(t) = \sqrt{\frac{1}{N}\sum_{\boldsymbol{x}\in\Omega} |\omega_c(\boldsymbol{x},t) - \omega_e(\boldsymbol{x},t)|^2}, \tag{13}$$

where N stands for the whole image pixel number, and where the subscripts $\boldsymbol{c}$ and $\boldsymbol{e}$ stand for the groundtruth field and the estimated field, respectively.

3.3 Results

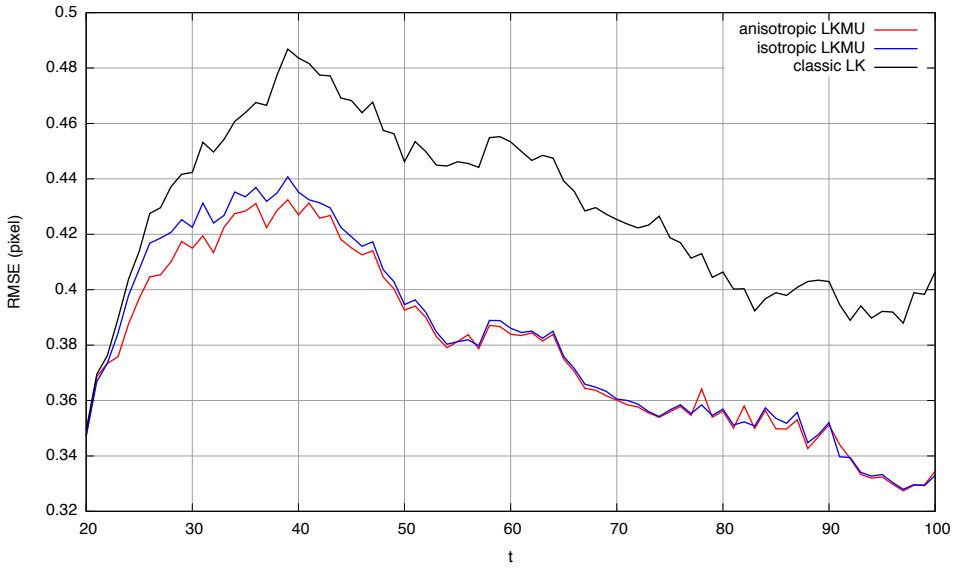

(a)

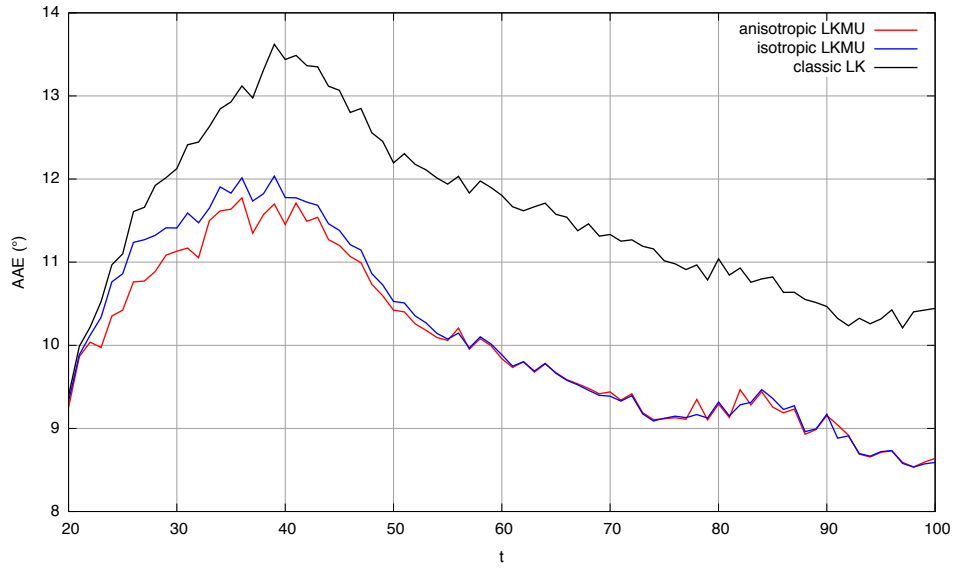

(b)

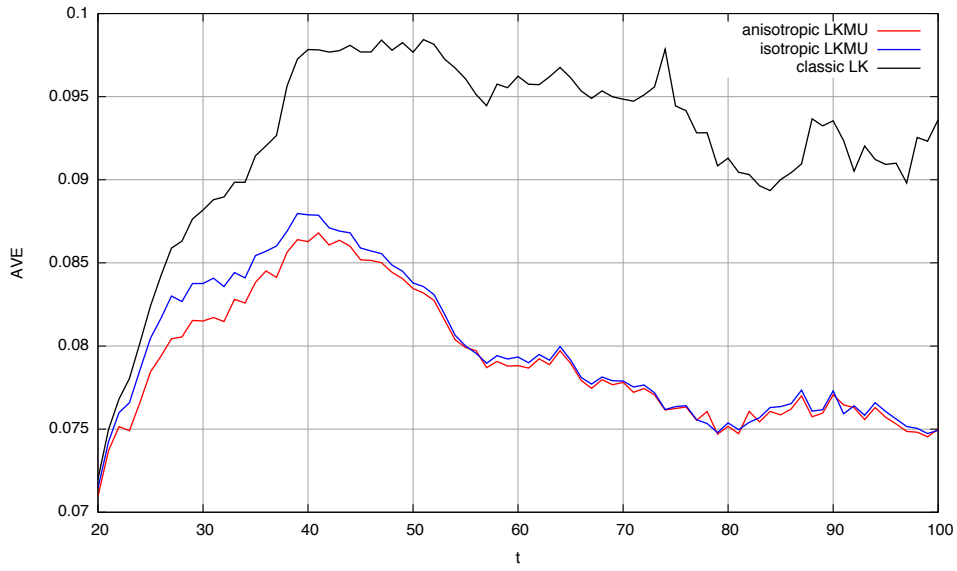

(c)

Fig. 2 RMSE (a), AAE (b) and AVE (c) versus time for the three methods applied to scalar images. The classic LK method is the brightness consistency based Lucas-Kanade resolution (black line). LKMU is the stochastic transport equation based Lucas-Kanade resolution (blue and red lines).

The figure 2 shows the RMSE, AAE and AVE time evolution for the scalar sequence (frames 20 to 100). The novel data term based on the stochastic transport equation (isotropic and anisotropic LKMU) is compared to a simple brightness consistency model (classic LK).

As observed for the scalar image sequence, LKMU improves the estimation (around 16% of error reduction), which indicates that the motion uncertainty model better describes the flow behavior than a simple brightness consistency assumption. However when comparing the isotropic version of LKMU to the anisotropic version, differences can be pointed out between the two versions only up to t=50. This slight improvement provided by the anisotropic model might be related to the anisotropic distribution of the scalar during the first 50 time steps of the simulation. Based on the power spectra analysis shown in figure 4 we can confirm the improvement brought by our method from the large to the small scales compared to the classic Lucas-Kanade approach.

Concerning the particle image sequence, figure 3 also shows the RMSE, AAE and AVE time evolution (frames 20 to 100). As we can see LKMU slightly improves the estimation, but not significantly (around 2%-3% of error reduction). However in this case anisotropic LKMU is always better than isotropic LKMU. In both cases (scalar and particles) the best improvement is observed for the vorticity error. The proposed model can better catch the vortex structures.

Note that these synthetic cases are not necessarily relevant to simulate twin experiments with large-scale motion since the DNS provides the smallest fluid motion scales. However, the scalar and particles distributions could introduce some large scale and anisotropic effects. For the scalar case, LKMU gave better estimation by simulating the isotropic molecular diffusivity of the scalar (Sc = 0.7) via the diffusion tensor, which also explained no big differences between isotropic and anisotropic estimations after t=50 when the scalar was more homogeneously distributed. For the particle case, there was no real large-scale assumption (the size of the interrogation windows was small and the particle density was high), thus only slight differences were observed between LK and LKMU estimations and mainly explained by anisotropic effects.

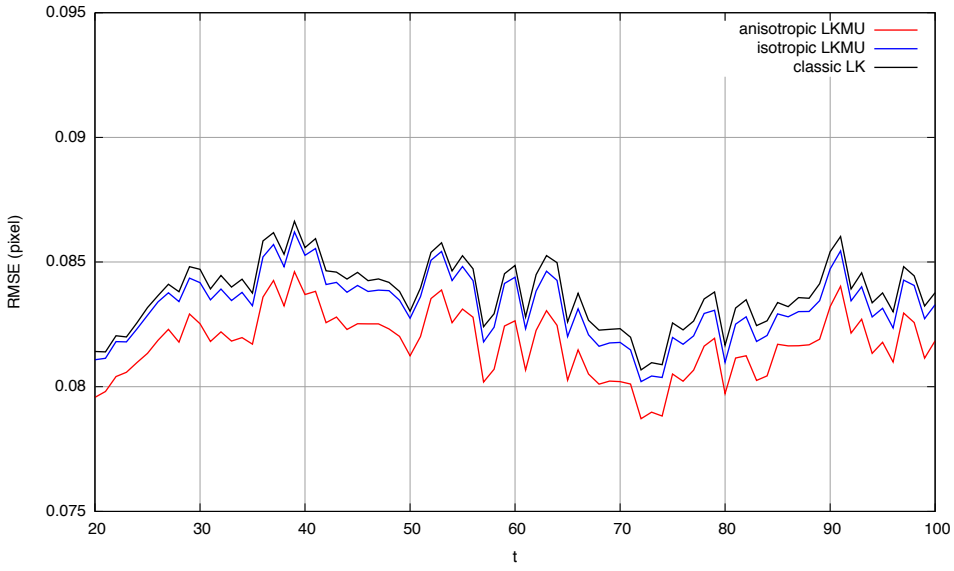

(a)

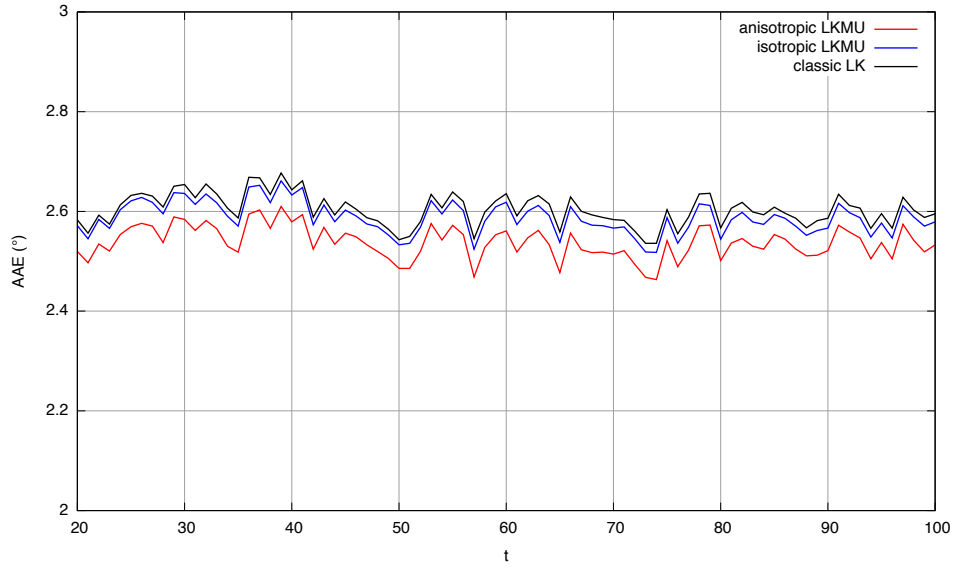

(b)

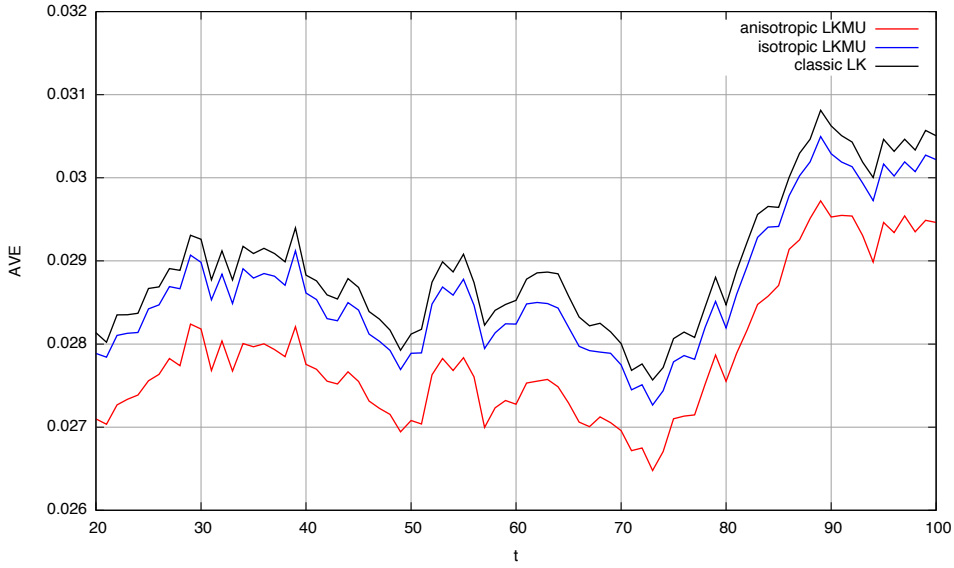

(c)

Fig. 3 RMSE (a), AAE (b) and AVE (c) versus time for the three methods applied to particle images.

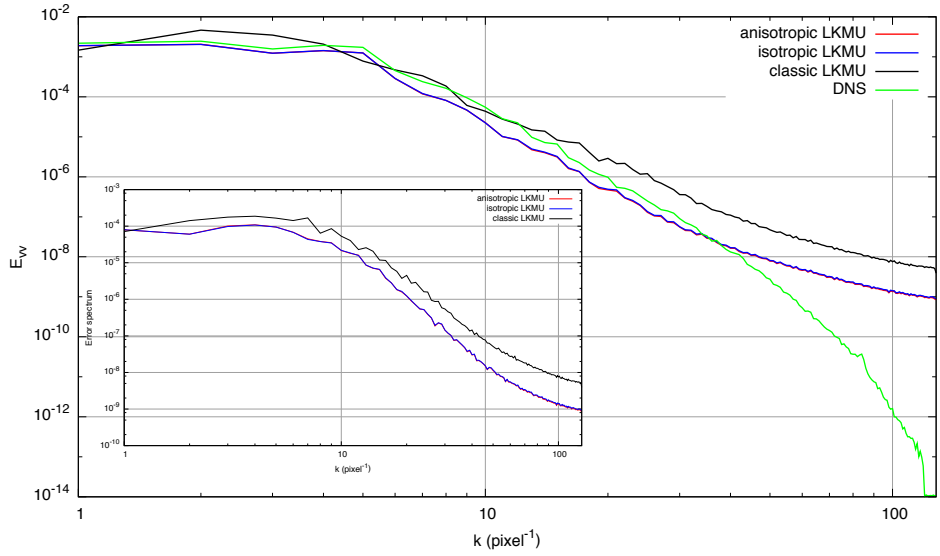

Fig. 4 Spectrum analysis of the turbulent velocity for DNS scalar image sequence at time t=100. Spectra of the error for the same data are shown in inset.

4. Mixing layer characterization

4.1 Experimental set-up

In this part we evaluate the performances of our method on real images of an isothermal mixing layer. This experiment was carried out in the wind tunnel HABV of Irstea-Rennes. The dimensions of the field of interest were 1m×1m. To enlighten this area we developed in collaboration with the french company EFFILUX an array of LEDs coupled with a linear Fresnel lens. The system emits a lightsheet of 1 cm thick at a wavelength around 465 nm. It was synchronized with a camera photron at 125 fps. A pulse duration of 1 ms was selected. The camera recorded 16 bits images of size 1024×1024 pixels. We tested two kinds of seeding: smoke and HFSB, see figure 6. The HFSB generator system was designed by LaVision. For the smoke we used a fog generator and designed two seeding ramps to contain the smoke in the lightsheet axis. The overall set-up is shown in figure 4. In figure 5 we display typical images we obtained for smoke and HFSB.

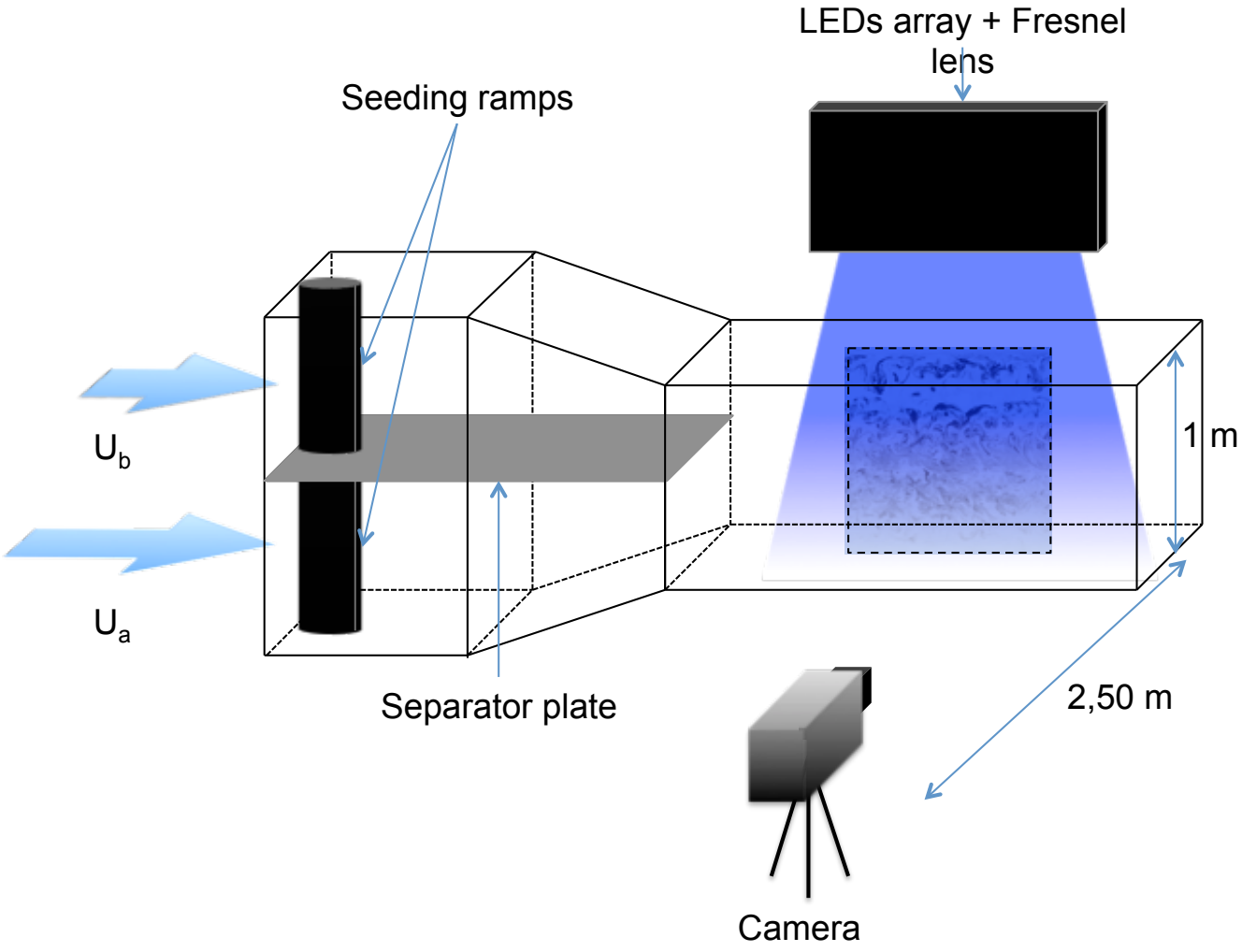

Fig. 5 Experimental set-up.

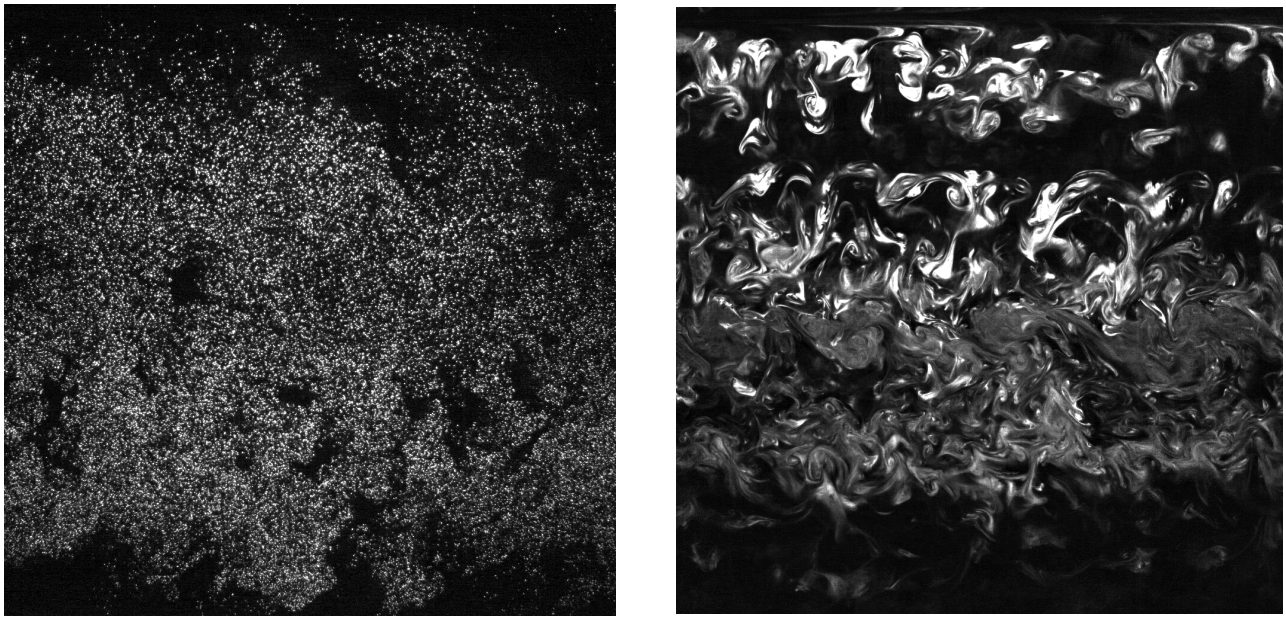

(a) HFSB (b) Smoke

Fig. 6 1024x1024 snapshots of smoke seeding (b) and HFSB seeding (a) in the mixing layer.

4.2 Results and discussion

Two sequences of velocity fields were computed with our new motion estimator : one for smoke seeding and one for HFSB seeding. From the mean velocity field exhibited in figure 7 we can derive some features of the mixing layer.

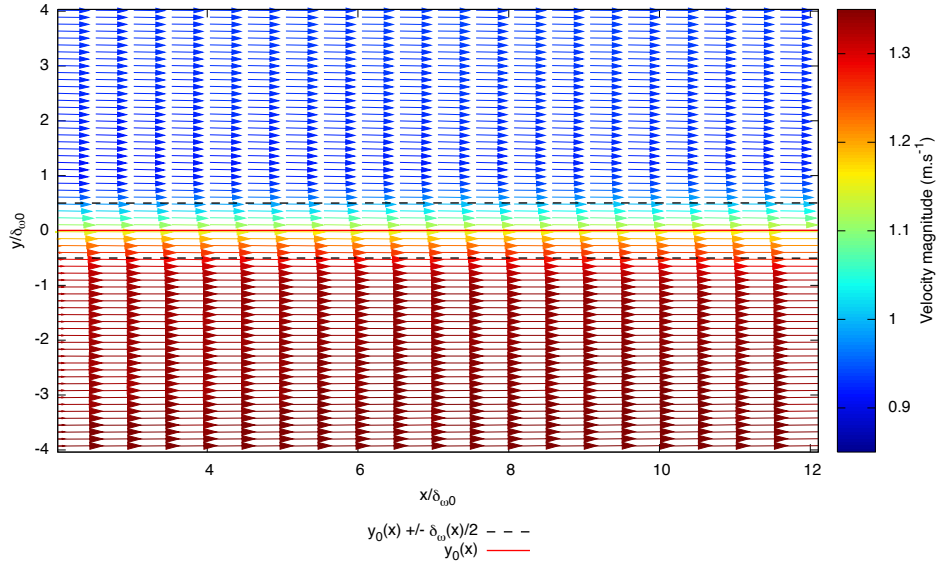

Fig. 7 Mean velocity field computed from instantaneous fields obtained with a smoke seeding (note that mean field for HFSB is quite similar). Black dashed lines delimit the vorticity thickness of the mixing layer. The red one represents the mixing layer axis.

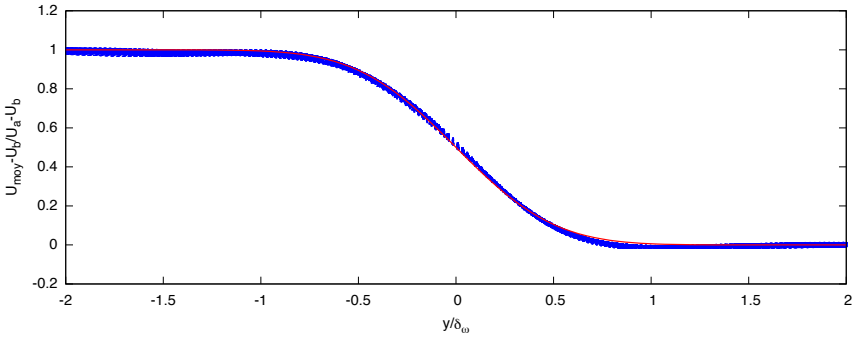

Fig. 8 Dimensionless stacked mean velocity profiles.

$$\overline{U}(x,y) = \frac{1}{2}\left(1 - erf\left(\frac{\sqrt{\pi}}{\delta_\omega(x)}(y - y_0(x))\right)\right)(U_a - U_b) + U_b \tag{14}$$

By fitting the law of (14) with the mean velocity field displayed in figure 7 and figure 8 we obtain characteristic parameters of the mixing layer. First we can retrieve the high velocity U_a and low velocity U_b which are very close to the wind tunnel set values reported in table 1. The two main first order parameters are the vorticity thickness $\delta_\omega(x)$ and the mixing layer axis $y_0(x)$. r is the ratio $\frac{U_b}{U_a}$ and $\lambda = \frac{1-r}{1+r}$. The good agreement between measurements and the similitude law means that we are in the auto-similarity zone. By analysing more deeply table 1 we see that smoke seeding measurements are very close to the set values. No differences can be noticed between the istotropic and anisotropic versions of the motion estimation method. Concerning the HFSB seeding we can notice that the velocities are slightly over-estimated. This may come from the expulsion flow of the bubble generator array of nozzles which gives an initial velocity to the bubbles and which could perturbate the wind tunnel flow. For these reasons we plane to study the influence of bubble generator nozzles on the wind tunnel flow.

Parameters	Wind tunnel setpoints	Smoke			HFSB (Anisotropic LKMU)
		Classic LK	Isotropic LKMU	Anisotropic LKMU	
$U_a\ (m.s^{-1})$	1.338	1.341	1.341	1.341	1.469
$U_b\ (m.s^{-1})$	0.914	0.925	0.925	0.925	1.05

r	0.68	0.69	0.69	0.69	0.71
λ	0.19	0.18	0.18	0.18	0.17

Tab. 1 Mixing layer parameters.

To validate the estimation of the vorticity thickness we compared our results to hot-wire anemometry measurements from (Heitz, 1999) and (Sodjavi, 2013) where mixing layers with similar λ were studied. The characteristic parameters are reported in table 2.

Parameters	Smoke	HFSB	(Sodjavi, 2013)	(Heitz, 1999)
λ	0.18	0.17	0.2	0.2
$\frac{\mathrm{d}\delta_\omega}{\mathrm{d}x}$	0.03	0,029	0.033	0.0336
σ	59,08	61,12	53,71	52.75
σ_0	10,63	10,39	10,74	10.55

Tab. 2 First-order characteristic parameters for different mixing layer with similar λ.

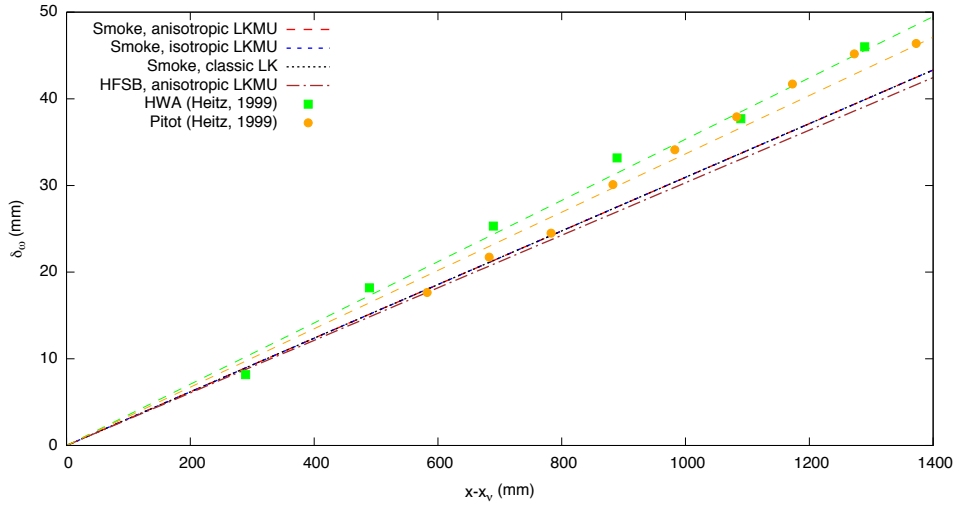

Fig. 9 Vorticity thickness evolution.

We also investigated turbulence intensities as shown in figure 10. We only displayed results from smoke image velocimetry, HFSB seeding results may present a bias error because of reasons mentioned above. We can observe that turbulence intensities from smoke image velocimetry were slightly larger compared to hot-wire anemometry measurements for a similar λ. This differences may be due to the differences between both mixing layers: one carried out in

the Irstea wind tunnel and perturbated by the seeding ramps, and the other formerly investigated with HWA in one of the wind tunnel of university of Poitiers (Heitz, 1999). Nevertheless the global trend of the curves was consistent.

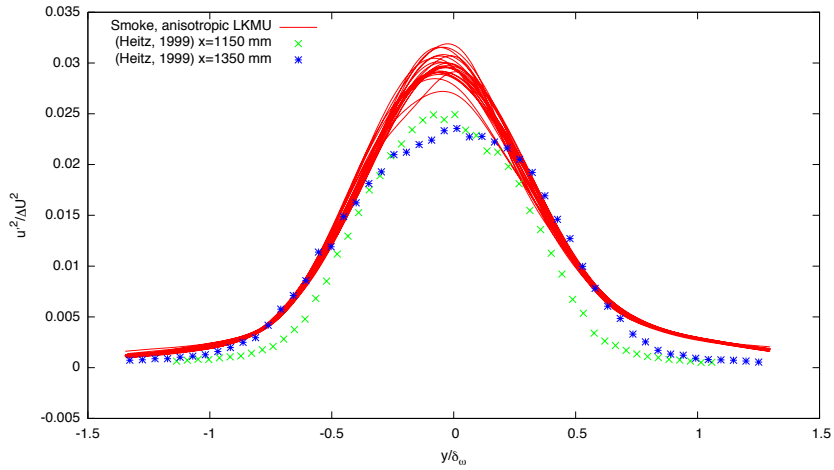

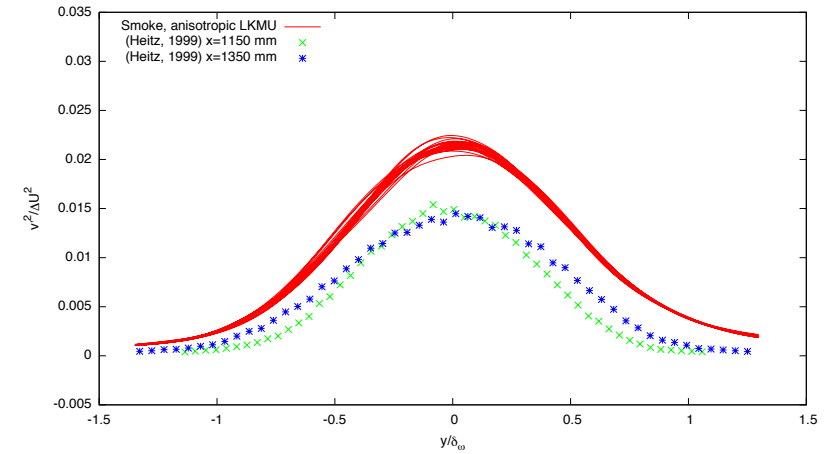

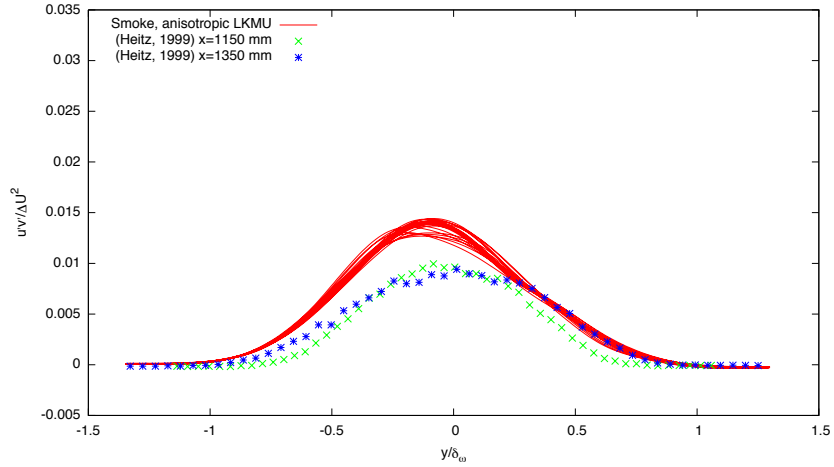

Fig. 10 Turbulence intensities $\frac{\overline{u'^2}}{\Delta U^2}$, $\frac{\overline{v'^2}}{\Delta U^2}$ and $\frac{\overline{u'v'}}{\Delta U^2}$ (from top to bottom). Comparisons between hot-wire anemometry measurements from Heitz (1999) for $\lambda = 0.2$ and smoke image velocimetry with anisotropic LKMU for $\lambda = 0.18$.

To test the accuracy limit of the method we investigated the kurtosis and skewness. As observed in figure 11 the proposed method is not able to properly retrieve the Kurtosis and the Skewness of the streamwise velocity component.

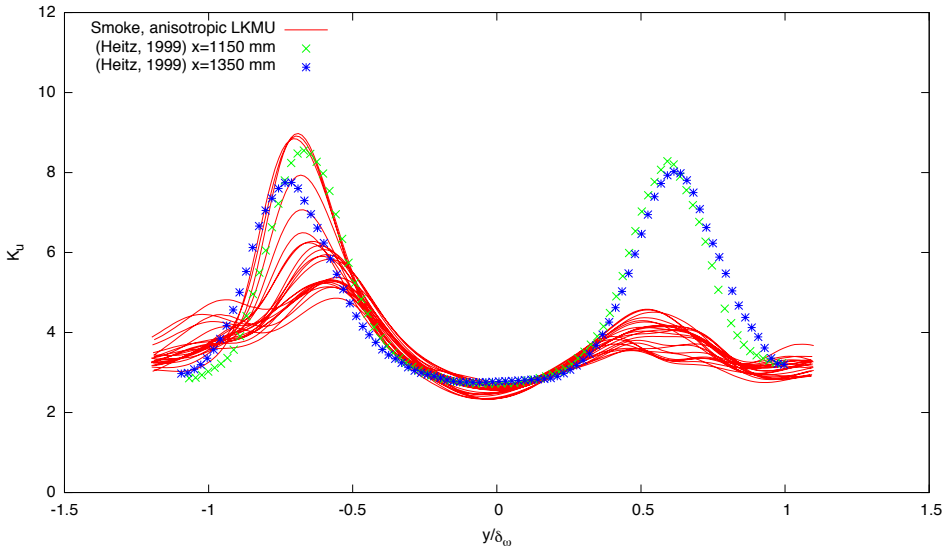

(a)

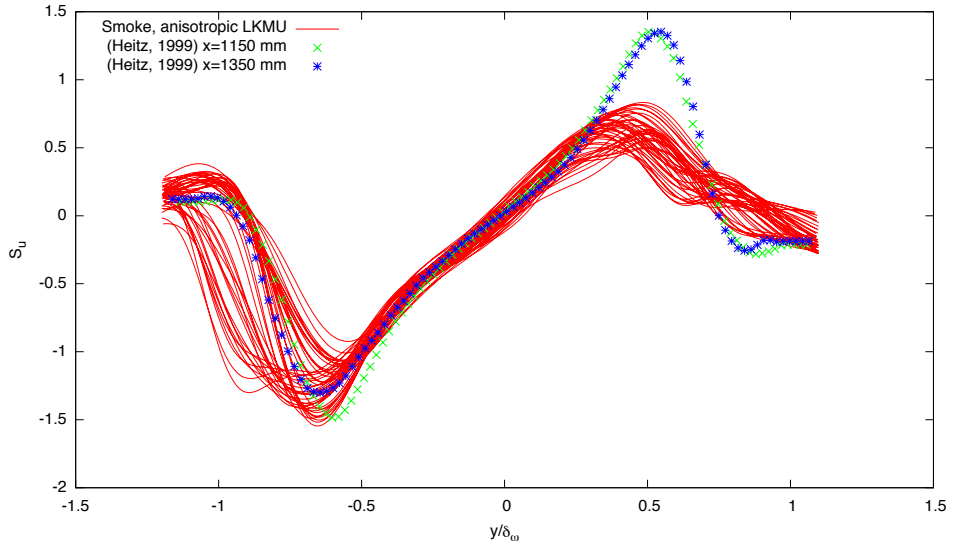

(b)

Fig. 11 Kurtosis, $\frac{\overline{u'^4}}{\overline{u'^2}^2}$ (a) and Skewness, $\frac{\overline{u'^3}}{\overline{u'^2}^{\frac{3}{2}}}$ (b).

5. Conclusion

In this paper we presented a new formulation of optical flow for large-scale turbulent flows analysis. This formulation is based on a data term derived from the stochastic transport equation of a passive scalar. This model takes into account the interactions between unresolved scales and resolved ones. Our new motion estimator improved the estimation results for the scalar and particles synthetic images.

We then performed a large-scale experiment on a mixing layer to evaluate the potential of our method with real images. Specific devices (illumination system, seeding system) were developed to carry out this large-scale experiment. First large-scale results are very encouraging, the main features of the mixing layer could be retrieved. It particularly shows that smoke image velocimetry measurements can be performed with an alternative motion estimation method.

However no significant effect of the stochastic data model could be observed with these real experiments. We will continue to investigate the potential effects of the stochastic data term on a synthetic 3D flow and on a new measurements campaign in our wind tunnel. There will be a deeper validation by performing comparison with HWA measurements carried out in the same flow (ie in the same wind tunnel) and by investigating possible perturbations introduced by the intrusive seeding systems. This study will let us precisely characterize large-scale turbulent flow estimations extracted from both smoke and HFSB image sequences.

References

Adrian R J (1991) Particle-imaging techniques for experimental fluid mechanics. Annual Review of Fluids Mechanics 23:261-304.

Bardina J, Ferziger J, Reynold W (1980) Improved subgrid-scale models for large-eddy simulation. American institute of aeronautics and astronautics, fluid and plasma dynamics conference, 13th, Snowmass, Colo.

Carlier J, Wieneke B (2005) Report 1 on production and diffusion of fluid mechanics images and data. Fluid project deliverable 1.2. European Project Fluid image analysis and description (FLUID) http://www.fluid.irisa.fr/.

Cassisa C, Simoëns S, Prinet V, Shao L (2011) Subgrid scale formulation of optical flow for the study of turbulent flow. Experiments in Fluids 51(6):1739-1754.

Chen X, Zillé P, Shao L, Corpetti T (2015) Optical flow for incompressible turbulence motion estimation. Experiments in Fluids 56:8.

Heitz D (1999) Etude expérimental du sillage d'un barreau cylindrique se développant dans une couche de mélange plane turbulente. Université de Poitiers.

Heitz D, Carlier J, Arroyo G (2007) Final report on the evaluation of the tasks of the workpackage 2. FLUID project deliverable 5.4. Technical report, INRIA – Cemagref.

Heitz D, Mémin E, Schnörr C (2010) Variational fluid flow measurements from image sequences : synopsis and perspectives. Experiments in Fluids 48(3):369-393.

Horn B K P, Schunck B G (1981) Determining optical flow. Artificial Intelligence 17(1-3):185-203.

Lee J P, Kim H L, Lee S J (2011) Large-scale PIV measurements of ventilation flow inside the passenger compartment of a real car. Journal of Visualization.

Liu T, Shen L (2008) Fluid flow and optical flow. Journal of Fluid Mechanics 614:253-291 (2008).

Lucas B D, Kanade T (1981) An Iterative Image Registration Technique with an Application to Stereo Vision. Proceedings of Imaging Understanding Workshop, pp. 121-130.

Mémin E (2014) Fluid flow dynamics under location uncertainty. Geophysical & Astrophysical Fluid Dynamics, 108:2 pp.119-146.

Scarano F, Ghaemi S, Caridi G C A, Bosbach J, Dierksheide U, Schiacchitano A (2015) On the use of heliumfilled soap bubbles for large-scale tomographic PIV in wind tunnel experiments. Experiments in Fluids 56:42.

Schanz D, Huhn F, Gesemann S, Dierksheide U, van de Meerendonk R, Manovski P, Schröder A (2016) Towards high-resolution 3D flow field measurements at cubic meter scales. 18th International Symposium on the Application of Laser and Imaging Techniques to Fluid Mechanics.

Sodjavi K (2013) Etude expérimentale de la turbulence dans une couche de mélange anisotherme. Université de Rennes 1.

Resseguier V, Mémin E, Chapron B (2017) Geophysical flows under location uncertainty, Part I-Random transport and general models. Geophysical & Astrophysical Fluid Dynamics 111:3 pp.149-176.

Zillé P, Corpetti T, Shao L, Chen X (2014) Observation models based on scale interactions for optical flow estimation. IEEE Transactions on Image Processing, 23(8):3281-3293.